Title	Photonic signal processing for inverse synthetic aperture radar imaging.
Author(s)	Riza, Nabeel A.; Pape, Dennis R.
Publication date	1998-08-25
Original citation	Riza, N. A. and Pape, D. R. (1998) 'Photonic signal processing for inverse synthetic aperture radar imaging', Proceedings of SPIE, 3388, Advances in Optical Information Processing VIII, Aerospace/Defense Sensing and Controls, Orlando, Florida, United States. doi: 10.1117/12.319435
Type of publication	Conference item
Link to publisher's version	http://dx.doi.org/10.1117/12.319435 Access to the full text of the published version may require a subscription.
Rights	© 1998 Society of Photo-Optical Instrumentation Engineers (SPIE). One print or electronic copy may be made for personal use only. Systematic reproduction and distribution, duplication of any material in this paper for a fee or for commercial purposes, or modification of the content of the paper are prohibited.
Item downloaded from	http://hdl.handle.net/10468/10182

PROCEEDINGS OF SPIE

Photonic signal processing for inverse synthetic aperture radar imaging

Riza, Nabeel, Pape, Dennis

SPIE.

Photonic Signal Processing for Inverse Synthetic Aperture Radar Imaging

Nabeel A. Riza[*]

Center for Research and Education in Optics and Lasers (CREOL)
and the Department of Electrical and Computer Engineering
University of Central Florida

Dennis R. Pape[#]

Photonic Systems Incorporated

ABSTRACT

A robust signal processor, capable of handling a multitude of signal processing functions over a wide instantaneous signal bandwidth is needed for future military systems where shared sensor and signal processing resources will be employed. We investigated a novel two dimensional acousto-optic (AO) processor capable of real-time multifunction signal processing. We developed the specifications for an optoelectronic ISAR image formation processor for ship imaging based upon the AN/APS-137(H) Airborne Radar. The baseline processor is designed for high resolution imaging - slant range resolution of 0.3 m and cross range resolution of 1.2 m over 30 m X 30 m window. The optical design of the processor is based on an optically efficient, in-line, high stability, two dimensional interferometer using four acousto-optic devices invented by Riza[1]. We developed specifications for the processor components, including light source, lenses, photodetector array, and Bragg cells including a mutichannel Brag cell to improve processor bandwidth and reduce its size. We showed that all of these components are commercially available. We breadboarded a narrow bandwidth version of the processor and demonstrated its main operating features. We showed experimentally that the processor has simultaneous spatial carrier generation capability that is controllable with high phase stability and excellent fringe visibility.

Keywords: Acousto-optic processor, inverse synthetic aperture radar imaging.

1. INTRODUCTION

Future naval systems will reduce the number of separate shipboard and airborne antennas by sharing sensor, receiver, and signal processing resources. A robust signal processor, capable of handling a multitude of signal processing functions over a wide instantaneous signal bandwidth is needed. In this paper, we investigated a novel two dimensional acousto-optic (AO) processor capable of real-time multifunction signal processing [1]. The effort described here concentrated on applying our processor to inverse synthetic aperture radar (ISAR) image formation. We showed that the necessary signal processing steps required for ISAR image formation are equivalent to calculating the ambiguity function of each radar return and summing the results. We developed an AO processor concept that generates the ambiguity surface for two input signals, where in this case, the coordinates of the time delay and Doppler frequency format are the x and y coordinates of the processor's output CCD array. We showed that the desired ambiguity function rides on a spatial carrier that is used for bias removal. A restriction on recovering Doppler information using this Fourier analysis approach is that the Doppler frequency of the return should not change during the integration period T_d. If the spectrum does change during this time then the Fourier transform is smeared and the resolution of the image is degraded in the Doppler frequency direction. We showed, however, that we can control the time-window over which we perform the Doppler filtering by controlling the processor integration period T_d. We also investigated time-frequency transform techniques (in particular wavelet transforms) for improving ISAR imagery.

We developed the specifications for an optoelectronic ISAR image formation processor for ship imaging based upon the Texas Instruments AN/APS-137(H) Airborne Radar. The baseline processor is designed for high resolution imaging - slant range resolution of 0.3 m and cross range resolution of 1.2 m over a 30 m X 30 m window. The optical design of the processor is based on a newly invented optically efficient, in-line, high stability, two dimensional interferometer using four acousto-optic devices [1]. The processor provides several simultaneous features, e.g., mechanical stability, processing generality, high

---

[*] CREOL/UCF, 4000 Central Florida Boulevard, P. O. Box 162700, Rm 280, Orlando, FL 32816-2700, Tel: 407-823-6829; Fax: 407-823-3354, email: riza@creol.ucf.edu.
[#] Photonic Systems Incorporated, 1800 Penn Street, Suite 6, Melbourne, FL 32901, Tel: (407) 984-8181, Fax: (407) 952-7748, email:dpape@photon-sys.com.

62

Part of the SPIE Conference on Advances in Optical Information Processing VIII
Orlando, Florida ● April 1998 ● SPIE Vol. 3388 ● 0277-786X/98/$10.00

dynamic range capability, ease in bias removal, and complex signal input ports, that were to a certain degree limited in previous architectures. The design is based on the mechanically stable in-line 2-D AO interferometer demonstrated previously for 2-D scanning beam control for microwave phased array antennas [2-4]. The stable interferometric nature of the system with four independent complex signal input ports results in the output desired term having a minimum number of undesired bias terms, leading to a high dynamic range design. Furthermore, the desired output term can be generated on a spatial carrier of any desired frequency and direction by simply changing the carrier frequencies driving the four Bragg cells; thus facilitating bias subtraction and post-processing procedures without requiring additional beam deflecting optics in the system. The AO processor makes efficient use of the input laser light, thus alleviating to some extent, the inefficiency in the double diffraction-cascade nature of the design. Via the simple technique of Bragg cell carrier offset adjustments, the processor can generate the desired high dynamic range interferometric output on a chosen spatial carrier that is required for bias removal and electronic post-processing.

We developed the specifications for the optoelectronic components for the processor, including light source, lenses, photodetector array, and Bragg cells including a mutichannel Bragg cell to improve processor bandwidth and reduce its size. We showed that all of these components are commercially available. We breadboarded a narrow bandwidth version of the processor and demonstrated its main operating features. We showed that the processor does indeed have simultaneous spatial carrier generation capability that is controllable with high phase stability and excellent fringe visability. In summary, the research effort described in this paper has resulted in an innovative acousto-optic signal processing architecture for ISAR ship image formation that is ideally suited to airborne applications where size, weight, and power are important performance parameters.

2. ISAR IMAGE FORMATION USING AN OPTOELECTRONIC PROCESSOR

There are a number of different viewpoints that can be taken in developing a signal processing algorithm that reduces ISAR returns to two-dimensional imagery. We show here that the necessary signal processing steps required for ISAR image formation are equivalent to calculating the ambiguity function of each radar return and summing the results. We describe a novel optoelectronic processor that produces ISAR images using this technique. A restriction on recovering Doppler information using this Fourier analysis approach, however, is that the Doppler frequency of the return should not change during the integration period T_d. We also discuss time-frequency transform techniques (in particular wavelet transforms) for improving ISAR imagery along with their optoelectronic implementation.
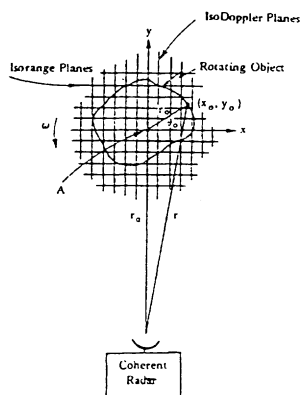

Fig. 1 Shows the relationship between a fixed coherent radar and the rotating object being imaged, i.e., ISAR Imaging [5].

The object is illuminated throughout the imaging process by a radar periodically pulsed during the movement of the object. The coordinate system for ISAR image formation is also shown in the figure. Points equidistant from the radar are located on successive concentric arcs across the object. If the distance to the object is much larger than the size of the object, then these arcs become isorange planes as shown in the figure. By measuring the time-delay between a transmitted and reflected radar pulse, each point scatterer within the object can be associated with a particular isorange plane. The exact position of a scatterer on a particular isorange plane can be resolved by noting that points located on planes equidistant from the center of rotation of the object yield reflected radar pulses with equal Doppler shifts. Isorange planes of equal time-delay and isoDoppler planes of equal Doppler shift form an unambiguous two-dimensional grid over the object. Each point scatterer

63

within the object can thus be unambiguously located by simultaneously measuring the time delay and Doppler shift of the pulse reflected from the scatterer. Since an extended object is a collection of point scatterers, an image of the object can be formed by mapping the intensity of all of the reflected radar pulses in a two-dimensional time-delay/Doppler space.

The time-delay measurement can be performed by processing the received radar pulse with a matched filter in the time domain. The output of a time domain matched filter is a cross correlation between the received signal and a time-delayed replica of the transmitted signal. The cross correlation between a return s(t) from a single point scatterer and the delayed replica or reference signal r, in its symmetric form, may be written as:

$$C(\tau) = \int_{-\infty}^{+\infty} s(t) \cdot r^*(t-\tau) \cdot dt = \int_{-\infty}^{+\infty} s(t+\tfrac{\tau}{2}) \cdot r^*(t-\tfrac{\tau}{2}) \cdot dt. \qquad (1)$$

The cross correlation function has its maximum when the (known) time-delay of the replica is the same as the (unknown) time-delay of the return.

2.1 Fourier Transform Analysis

The Doppler shift measurement can be performed simultaneously with the time-delay measurement by processing a series of received radar pulses with a time/frequency domain matched filter, i.e., by performing an ambiguity function measurement:

$$A(\tau, f) = \int_T s(t+\tfrac{\tau}{2}) \, r^*(t-\tfrac{\tau}{2}) \cdot e^{-i2\pi ft} \cdot dt = \int_T S^*(v) \cdot R(v+f) \cdot e^{-i2\pi vt} \cdot dv, \qquad (2)$$

where the integral describes the Fourier transform of the correlation between the received radar returns s(t) and the reference transmitted radar pulse r in the time domain and the Fourier transform of the product of the received radar signal spectrum S and the reference transmitted radar pulse spectrum R in the Fourier domain. The ambiguity function has its maximum when the (known) time-delay of the replica is the same as the (unknown) time-delay of the return and where the Doppler shift of the return is the same as the transform frequency. Since each point scatterer on the object has a unique time-delay and Doppler shift, a display of all of the ambiguity function measurements of all of the point scatterers results in an image of the object in two-dimensional time-delay/Doppler space. The integration time T required for the Doppler shift measurement is much longer than a single pulse width. We thus require that the point scatterer have constant time-delay and Doppler shift during the Doppler measurement. We also require that the PRF of the radar meet the Nyquist sampling criterion and that the coherent integration time T must, at a minimum, be equal to the inverse of the Doppler frequency.

2.2 Wavelet Transform Analysis

A restriction on recovering Doppler information using the process described above is that the Doppler frequency of the return should not change during the integration period T_d. If the spectrum does change during this time (which it does because of target motion) then the Fourier transform is smeared and the resolution of the image is degraded in the Doppler frequency direction. One approach to alleviating this problem is to perform a short-time Fourier transform. This can be easily accomplished with the proposed processor. Here we control the time-window over which we perform the Doppler filtering by controlling the processor integration period T_d. There is obviously a tradeoff in frequency resolution using this approach, however. A short integration time T_d results in poor frequency resolution. Nevertheless, the processor has the flexibility of controlling integration time and we propose to exploit this feature. The Fourier transform process of Equation (2) decomposes the range compressed return into a series of Fourier basis functions $e^{-i2\pi ft}$ that have infinite temporal extent. The Fourier transform thus determines the spectral content of the signal but does not provide any temporal information. Where the spectral information is time-varying, as in the ISAR process, infinite temporal extent basis functions are inadequate. An alternative processing technique uses the Joint Time-Frequency transform (JTFT) implemented with wavelet transforms [6]. In this case, the conventional Fourier transform for Doppler processing is replaced by the JTFT, and the conventional 2-D range-Doppler Fourier frame becomes a 3-D time-range-Doppler cube. Now, by sampling in time, a time sequence of 2-D range-Doppler images can be seen. The wavelet transform decomposes the signal into a series of basis functions called daughter wavelets that are the dilations and translations of a unique function h(t) called a mother wavelet. The daughter wavelets are:

$$h_{a,b}(t) = \tfrac{1}{\sqrt{a}} \cdot h\left(\tfrac{t-b}{a}\right), \qquad (3)$$

where "a" is a dilation or scale parameter and "b" is a translation parameter. The wavelet transform of a signal f(t) is then:

$$W_f(a,b) = \int f(t) \cdot h^*_{a,b}(t) \cdot dt = \tfrac{1}{\sqrt{a}} \int f(t) \cdot h^*_{a,b}\left(\tfrac{t-b}{a}\right) \cdot dt ,$$ (4)

which is a correlation between the function $f(t)$ and the mother wavelet $h_{a,b}(t)$ scaled by a dilation factor "a" and shifted by a time constant "b". The discrete wavelet transform is usually performed. Here the scale is $a = a_0^m$, where a_0 is the discrete scale step size (usually 2), and b $= n b_0 \cdot a_0^m$ where $b_0 \cdot a_0^m$ is the discrete translation step size (usually 2^m) and m and n are integers.

A particularly useful mother wavelet for frequency decomposition is a windowed Gaussian function (Morlet mother wavelet):

$$h(t) = \tfrac{1}{\pi^{1/4}} \cdot e^{-ikt} \cdot e^{-\frac{t^2}{2}} ,$$ (5)

$$k = \pi \cdot \sqrt{\tfrac{2}{\ln 2}} .$$ (6)

The daughter wavelets are then dilations and translations of this mother wavelet. When the scale factor "a" is small then the window is narrow and the frequency of the wavelet is high. When the scale is large then the window is wider but the frequency is lower. Thus we have a transform where the temporal extent of the basis function varies inversely as a function of the frequency. In this way the time/frequency resolution problem of the Fourier transform analysis for ISAR image formation as described above is mitigated.

2.3 Optical Implementation of the Ambiguity Function ISAR Processor

Figures 2 and 3 show our two dimensional acousto-optic ISAR image formation processor. Fig. 2 shows a three dimensional view and Fig. 3 shows the detailed top and side views. AOD1 is driven by the reference signal $r(t)$ (a replica of the transmitted radar signal) mixed with a carrier frequency $\omega_c + \delta\omega_1$ (where ω_c is the gross AOD carrier frequency and $\delta\omega_1$ is a small carrier offset frequency adjustment.). The signal $s_1(t)$ input to AOD1 is then:

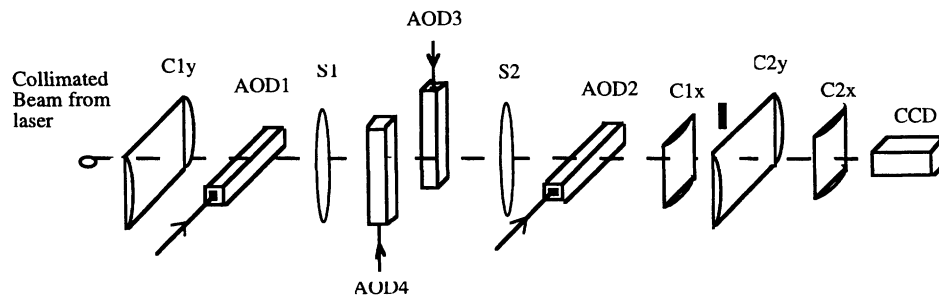$$s_1(t) = r(t) \cdot \cos\left[(\omega_c + \delta\omega_1)t\right] .$$ (7)

Figure 2: Three dimensional view of the acousto-optic ISAR image formation processor.

AOD1 generates a +1 order positive Doppler shifted and spatially deflected beam in the x-direction that is labeled as +1x, while the undiffracted DC beam from AOD1 is labeled as DC. The spherical lens S1 takes the +1x diffracted and DC beams and forms vertical Bragg matched light slits (along the y-direction) in AOD3 and AOD4, respectively. AOD3 and AOD4 are driven by slow chirp rate down and up chirp signals respectively:

$$s_3(t) = 2 \cdot a_1 \cdot \cos\left[(\omega_c + \delta\omega_3)t - \pi b t^2\right] \text{ and } s_4(t) = 2 \cdot a_1 \cdot \cos\left[(\omega_c + \delta\omega_4)t + \pi b t^2\right] .$$ (8)

The chirp rate is given by $b = (B_{AOD}/T_s)$, where B_{AOD} is the bandwidth of AOD3 and AOD4, and T_s is the duration of the chirp. Typically, $T_s = kT_a$, where k is an integer and T_a is the time aperture of the AOD. The +1x beam from AOD1 generates a negative Doppler -1y diffracted beam along the y-direction from AOD3. This double diffracted beam (from AOD1 and AOD3) is called +1x , -1y. The DC beam from AOD1 generates a positive Doppler shifted, y-direction deflected, diffracted beam from AOD4 labeled +1y. AOD2 is driven by the radar return signal $s(t)$ mixed in the same way as $r(t)$ except with a different carrier offset frequency:
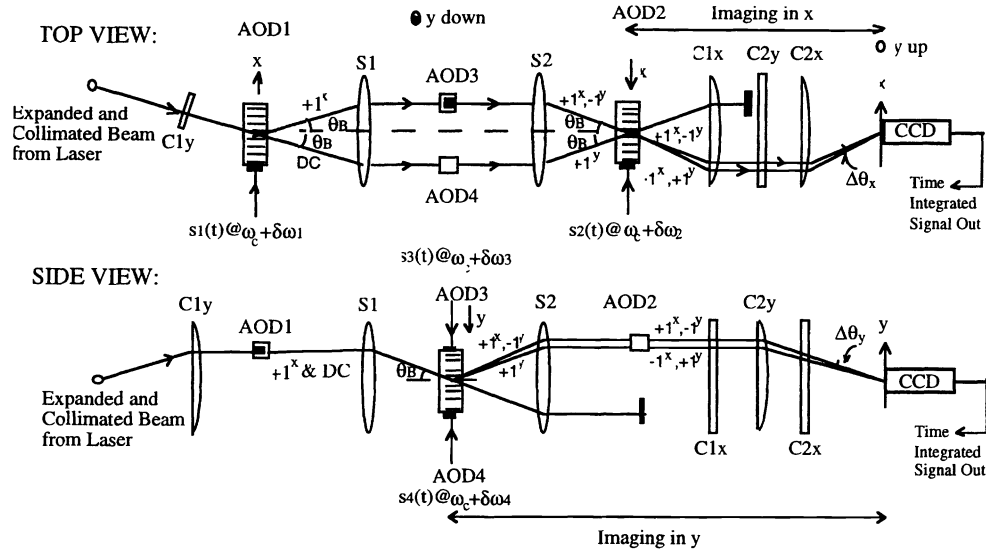
Figure 3: Top and side views of the acousto-optic ISAR image formation processor. The figure shows the various Bragg diffracted beams in the system, and the final beam pair that interferes on the 2-D time integrating detector shown here as a CCD.

$$s_2(t) = s(t) \cdot \cos\left[(\omega_c + \delta\omega_2)t\right].$$

(9)

The +1y beam is Bragg matched to AOD2 (in the x-direction), and generates a negative Doppler shifted -1x diffracted beam along the x-direction. This double diffracted beam (from AOD4 and AOD2) is called -1x , +1y , and it passes through the series of cylindrical lenses C1x , C2y , and C2x to be incident on the 2-D time integrating detector array. The +1x , -1y double diffraction beam from AOD1 and AOD3 Bragg diffractions passes through AOD2 essentially unaffected. This beam then also passes through the series of cylindrical lenses C1x , C2y , and C2x to be incident on the 2-D detector array. Thus, the two doubly diffracted beams +1x,-1y and -1x,+1y interfere on the detector plane with orthogonal coordinates x and y. Note that the DC block spatial filter prevents the undiffracted light beam from hitting the detector array. Note also that the spherical lens pair S1 and S2 forms a 1:1 imaging system in x,y between the AOD1 plane and the AOD2 plane, thus maintaining Bragg matching conditions. The cylindrical lens pair lenses C1x , C2x forms a 1:Mx imaging system along the x-direction between the AOD2 acoustic axis and the detector plane x-axis. Mx is the magnification factor given by the ratio of the C2x cylinder focal length to the C1x cylinder focal length. Similarly, the sphere S2 and cylindrical lens C2y forms a 1:My imaging system along the y-direction between the AOD3/AOD4 acoustic axis and the detector plane y-axis. Here My is the magnification factor given by the ratio of the C2y cylinder focal length to the S2 sphere focal length. Thus, eventually, the signals fed to AOD1 and AOD2 appear as counter-propagating signals along the x-direction of the 2-D detector, while the signals fed to AOD3 and AOD4 appear as counter-propagating signals along the y-direction of the 2-D detector. Note that there are slight relative deflection angles $\Delta\theta x$ and $\Delta\theta y$ along the x and y directions, respectively, between the two interfering beams on the detector array. These deflection angles are generated through AOD carrier offset frequencies, and are used to generate a desired spatial carrier on the detector plane for bias removal and signal post-processing.

The AOD carrier frequencies are tuned so that no temporal variation in the light diffraction at the CCD output of the processor occurs:

$$\delta\omega_1 + \delta\omega_2 = \delta\omega_3 + \delta\omega_4.$$

(10)

The output CCD integrates the light pattern for a duration T_d , where $T_d > T_s$. The light intensity I (x,y) at the CCD is:

$$I(x,y) = \left| r(t - \tfrac{x}{v})e^{-j(\omega_c + \delta\omega_1)\left(t - \tfrac{x}{v}\right)} \cdot a_1 \cdot e^{-j\pi b\left(t - \tfrac{y}{v}\right)^2} \cdot e^{+j(\omega_c + \delta\omega_3)\left(t - \tfrac{y}{v}\right)} + s(t + \tfrac{x}{v})e^{+j(\omega_c + \delta\omega_2)\left(t + \tfrac{x}{v}\right)} \cdot a_1 \cdot e^{-j\pi b\left(t + \tfrac{y}{v}\right)^2} \cdot e^{-j(\omega_c + \delta\omega_4)\left(t + \tfrac{y}{v}\right)} \right|^2,$$

(11)

66

where we have used -1 and +1 order single-sideband diffracted light representations from AOD3 and AOD4, respectively.

The integrated interferometric term of Eq. (11) is:

$$Q(x,y) = 2 \cdot a_1^2 \cdot 2\,\mathrm{Re}\left\{ e^{j(\omega_x x + \omega_y y)} \int_0^T s(t + \tfrac{x}{v}) \cdot r^*(t - \tfrac{x}{v}) \cdot e^{-i2\pi\left(\frac{2by}{v}\right)t} \cdot dt \right\}, \tag{12}$$

where $\omega_x = (\delta\omega_2 - \delta\omega_1)/v$ and $\omega_y = (\delta\omega_3 - \delta\omega_4)/v$ are spatial carrier frequencies in the x and y directions, respectively. The time integrated bias term is given by

$$B(x,y) = |a_1|^2 \int_0^T \left[\left| r\left(t - \tfrac{x}{v}\right) \right|^2 + \left| s\left(t + \tfrac{x}{v}\right) \right|^2 \right] \cdot dt. \tag{13}$$

Comparing Equations (2) and (12), Equation (12) shows that the return radar pulse is matched filtered in the time-domain and the output is displayed across the x direction of the CCD array where the horizontal dimension of the CCD indicates time-delay $\tau = 2x/v$ and each element of the CCD in the horizontal direction is associated with a range bin. Equation (12) further shows that the signal in each range bin is match filtered in the frequency domain via the presence of a local oscillator at the CCD array with frequency $f = 2by/v$ which varies linearly across the vertical y dimension of the array. Thus, the x and y coordinates of the CCD represent time delay and Doppler frequency coordinates, respectively. The desired ISAR image rides on a spatial carrier that is used for bias removal and complex-valued processing. In this processor the signal in each range bin is effectively passed through a bank of continuous Doppler filters. The bank of filters ranges in frequency from 0 to $2by_{max}/v = 2bT_a$ where T_a is the time-aperture of Bragg cells AOD3 and AOD4. The number of resolvable frequencies is $2bT_dT_a$. Since bT_d (the chirp bandwidth) cannot be larger than the bandwidth of the cell plus the bandwidth of the signal, the maximum number of resolvable elements is T_aB, the time-bandwidth product of the Bragg cell. The bandwidth of each Doppler filter is then $1/T_d$ with a minimum value of $2b/B$. To process the ISAR radar signals, the acousto-optic processor shown in Figures 2 and 3 operates as follows. The received radar returns are fed to Bragg cell AOD1. At the same time as the first return enters AOD1, the replica of the transmitted pulse is launched into Bragg cell AOD2. This process (called range gating) is repeated at the PRF of the radar transmitter for the duration of the integration period. Experiments have shown that the maximum integration time for ship targets at this radar band (X band) is 0.5 s [7]. Integration times longer than this result in image blurring.

2.4 Optical Implementation of a Wavelet Transform ISAR Processor
The usual approach to optically implementing the wavelet transform is to perform the processing in the Fourier domain. The wavelet transform expressed in the Fourier domain is:

$$W_F(a,b) = \int F(f) \cdot H_{a,b}^*(f) df = \frac{1}{\sqrt{a}} \int F(f) \cdot H^*(af) \cdot e^{i2\pi fb} df \tag{14}$$
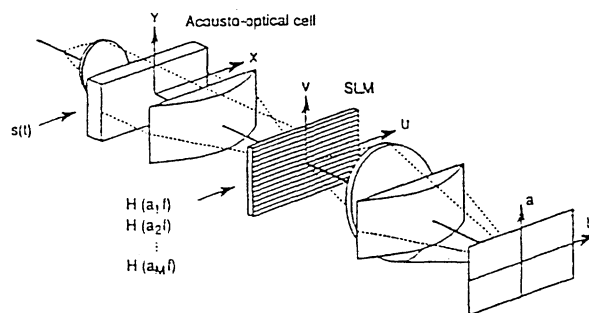

Figure 4: Acousto-Optic wavelet transform processor.

Thus the wavelet transform in the Fourier domain is an inner product between $F(f)$ and $H_{a,b}(f)$ and can be implemented by a bank of filters $H_{a,b}(f)$ in the Fourier plane. One can easily implement this optically with a two-dimensional acousto-optic

correlator as shown in Fig. 4 [8]. Here f(t) (labeled s(t) in the diagram) is input to an acousto-optic Bragg cell. A cylindrical lens performs a one-dimensional Fourier transform on f(t) producing the signal spectrum F(f) along the u dimension in the Fourier plane of the cylindrical lens. The filters H(af) are encoded in the Fourier plane in a two-dimensional spatial light modulator. The SLM is divided into horizontal filters, with the dilation factor "a" changing in the horizontal dimension for each filter. The spherocylindrical lens performs the inverse Fourier transform along the horizontal axis and images along the vertical axis in the output plane. The wavelet transform $W_f(a,b)$ appears in the output plane with the parameter "b" varying along the horizontal dimension and "a" varying along the vertical dimension. In this case the parameter "b" is continuous while "a" is discretized.

In the ISAR image formation process, the function F(f) in Equation (14), as shown in Equation (2), is the product of the received radar return spectrum S and a replica of the transmitted return spectrum R. In the processor shown in Fig. 2 this cross-correlation is performed by inputting the return in AOD1 and the replica of the transmitted signal in AOD2. The cross-correlation is displayed and integrated at the photodetector plane. In order to implement the wavelet transform in the Fourier domain we need to form the transform of the correlation and filter it with the daughter wavelet filter bank.

An alternate approach to optically implementing the wavelet transform is to perform the processing in the time domain (Equation 4). Here we need to cross-correlate the range-compressed returns with the mother wavelet $h_{a,b}(t)$ scaled by a dilation factor "a" and shifted by a time constant "b". These wavelets could be generated electronically and input to a multichannel Bragg cell in order that a series of scaled wavelets could be entered simultaneously. The optimum wavelet filter bank for either approach must be determined adaptively based upon the range-compressed returns.

3. ACOUSTO-OPTIC PROCESSOR COMPONENTS

With the wide selection of performance parameters available from optoelectronic devices, the processor shown in Fig. 2. could be configured to process ISAR data from a wide variety of data collection geometries. In this section we specify components for an ISAR radar used to image ship targets [7].

3.1 ISAR performance specifications

Two multimode maritime surveillance radar systems have been identified that this processor might be applied to - the Texas Instruments AN/APS - 137(V)/(H) Airborne Radar and the Westinghouse Norden Systems AN/APG -76 Multi-Mode Radar. In the open literature specifications are only available for the AN/APS - 137(H) Airborne Radar. These specifications, shown in Table I [9], will be used as the baseline for the design of the acousto-optic processor components.

Table I

AN/APS-137(H) Airborne Radar Specifications

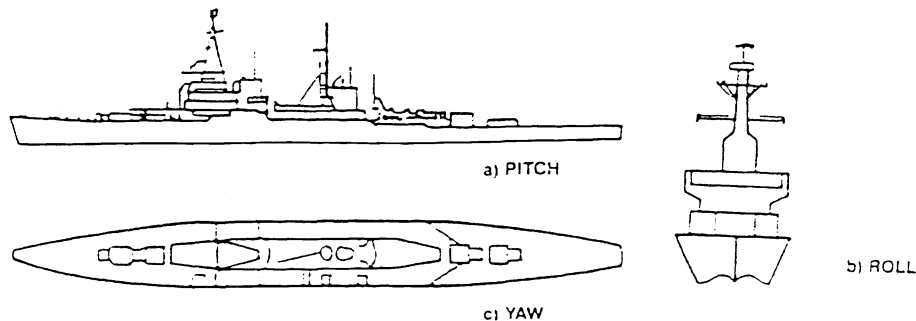| Center frequency	9.75 GHz	Pulsewidth	10 μs
Instantaneous bandwidth	500 MHz	PRF	5 kHz

a) PITCH

b) ROLL

c) YAW

Figure 5: ISAR image views produced by target pitch, roll, and yaw [10].

For ship targets, Fig. 5, where pitch, roll, or yaw causes rotational motion, the ISAR image plane is directed in a plane containing the radar line of sight vector and the rotational motion component [10]. We will assume, for this discussion, that the radar is used to image the ship using the roll rotational motion as shown in Fig. 6 [10]. The ISAR image plane then consists
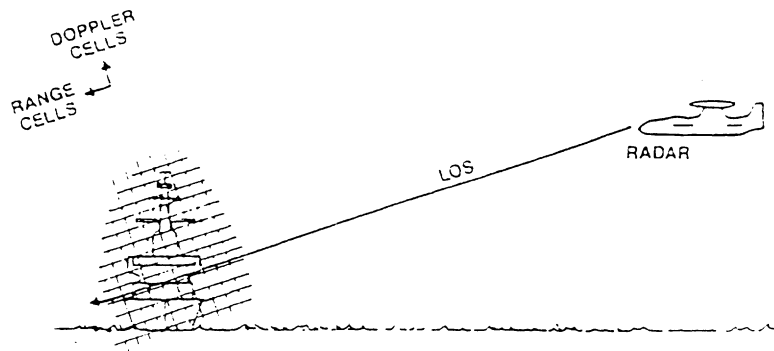
68

Figure 6: ISAR image plane with range and Doppler cells for ship target with roll [10].

of the ship's length W (assumed to be 30 m) for slant range and the ship's height H (assumed to be 30 m) for cross range (Doppler).

In its low resolution mode, the slant range resolution achievable with this radar is limited by the pulse width T of 10 μs. The low resolution mode slant range resolution ($\Delta r_{s, low}$) is: $\Delta r_{s,low}$=cT/2=1500 m.

With a 200 μs pulse repetition rate, a total of 20 slant range bins are available. In its high resolution mode, resolution in the slant range direction is achieved using pulse compression. The high resolution mode slant range resolution ($\Delta r_{s, high}$) with this 500 MHz bandwidth (B) radar is: $\Delta r_{s,low}$=c/(2B)=0.3 m.

Similarly, in this mode 100,000 range gates are available. We assume, however, that in the high resolution mode the ships gross position has already been determined. Since the ship is 30 m in width, 100 slant range bins will be required to capture the entire image of the ship. The Doppler gradient on the radar return is generated by the ship's pitch. In the worst-case sea-state 5 conditions, the predicted roll rate ω for a destroyer is 6.3°/s [7]. If its exposed height h above the surface is 30 m, the maximum Doppler bandwidth to be sampled following velocity correction to zero at the center of rotation is: f_D=(2/c)ωHf=214 Hz, where we have used f = 9.75 GHz. This is well below the 5 kHz radar PRF. The cross range resolution is given by: Δr_c = λ/(2Δθ), where Δθ is the angle through which the ship rotates during the coherent integration time. Migration through cross range cells is avoided if Δr_c > LΔθ/2 resulting in Δr_c > (λL/4)$^{1/2}$ = 1.22 m. The Doppler resolution of the system then will be: Δf_d = 2ωΔr$_c$/λ = 8.8 Hz.

We thus require 24 Doppler bins and a minimum coherent integration time of 114 ms. Integration times up to 0.5 s may be used without imaging blurring at this radar operating frequency [7].

Table II
Baseline ISAR Design Parameters

Center frequency	9.75 GHz	Slant range bins	100
Instantaneous bandwidth	500 MHz	Cross range resolution	1.2 m
Pulsewidth	10 μs	Cross range window	30 m
PRF	5 kHz	Cross range (Doppler) bins	24
Coherent integration time	0.5 s	Maximum Doppler bandwidth	214 Hz
Slant range resolution	0.3 m	Doppler resolution	8.8 Hz
Slant range window	30 m		

A summary of the baseline ISAR design parameters for a ship target imaging radar like the AN/APS(H) - 137 which will be used to specify the optoelectronic components of the ISAR processor is given in Table II.

3.2 Acousto-Optic Bragg Cells

The design and performance of the system shown in Fig. 2 is highly dependent on the types of Bragg cells used in the processor. In order to have the highest possible processing bandwidth, it is critical that all Bragg cells that fall in the spatial Fourier transform planes of the input signals have high (> 50 %) fractional bandwidths. Bragg cells AOD1 and AOD2 are used to cross correlate the radar return pulse with a replica of the transmitted pulse. These cells must support a bandwidth of

69

500 MHz. In order to have 50% fractional bandwidth, we require these cells to have a center frequency of at least 750 MHz. These cells must also yield a maximum of 100 resolvable range bins. Since the correlator has a resolution of $1/B$, the time aperture of these two Bragg cells must be at least $1/B \times 100 = 0.2$ μs. A Bragg cell of this type is commercially available from a number of sources. For example, Brimrose Corporation offers a model GPD-80-50, a 500 MHz bandwidth, 0.7 μs aperture cell with an efficiency of 35%/W [11]. This unit has an active aperture of 0.076×5 mm. Bragg cells AOD3 and AOD4 are used for Doppler filtering. The diffracted light from these two Bragg cells acts as a spatially distributed oscillator whose frequency $f = 2by/v$ (see Equation 8 and subsequent discussion) varies linearly with chirp rate b and distance y in the photodetector plane. The frequency range of the oscillator is 0 to $2by_{max}/v = 2 bT_a$, where T_a is the time aperture of the Bragg cell. The pulse compressed radar signal, produced by the correlation of the radar return with its reference in Bragg cells AOD1 and AOD2, respectively, is Doppler filtered when it illuminates the CCD detector array which is also illuminated with the distributed oscillator array. Since the maximum Doppler frequency to be detected is 214 Hz, the time-bandwidth product at the CCD plane must be 214 - 107 at the Bragg cell since the signals are counterpropagating. Suppose the time-aperture of the Bragg cells is 1 μs. We then require a Bragg cell with a bandwidth of 107 MHz. The chirp rate must be $b = 214$ Hz/(2·1 μs) = 107 MHz/s. One method for improving the processor design in terms of bandwidth and system size is to replace these single channel Bragg cells by an independently driven two-channel Bragg cell. AOD3 is illuminated by the diffracted optical beam from AOD1. AOD4 is illuminated by the DC optical beam from AOD1. The Bragg angle of AOD1 coupled with the focal length of spherical lens S1 determines the physical separation between AOD3 and AOD4. A short focal length S1 lens is desirable because 1) it makes the processor shorter and therefore more stable and 2) it minimizes the width of the optical beam appearing at AOD3. The latter is important because the acoustic beam of AOD3 is narrow and in order to achieve maximum optical throughput, the width of the optical beam must be less than the acoustic beam height. We compared the performance of 6 different 107 MHz bandwidth, 1 μs time-aperture acousto-optic Bragg cell designs. We investigated designs using three different acoustic modes in Gallium Phosphide (GaP), as well as modes in Tellurium Dioxide (TeO$_2$), Lead Molybdate (PbMoO$_4$), and Lithium Niobate (LiNbO$_3$). The results of this calculation are shown in Table III.

Table III
ISAR Bragg Cell Design Comparison for Bragg Cells AOD3 and AOD4

MATERIAL PARAMETERS						
Crystal	GaP	GaP	GaP	GaP	PbMo$_4$	LiNbO$_3$
Crystal glass	Cubic	Cubic	Cubic	Tetragonal 422	Tetragonal 4/m	Trigonal 3m
Acoustic mode	L [1,-1, 0]	S [1, -1, 0]	S [1, -1, 0]	L[001]	L[001]	L[100]
Optical illumination	[1, 1, -2]	[1, 1, 0]	[1, 1, 1]	[010]	[010]	[0, -0.5878, 0.809]
Curvature plane	[1,-1,0]/[1,1,1]	[1,-1,0]/[0,0,1]	[1,-1,0]/[1,1,-2]	[001]/[100]	[001]/[100]	[100]/[0,0.809,0.5878]
Index of refraction	3.31	3.31	3.31	2.26	2.39	2.20
Density (g/cm^3)	4.13	4.13	4.13	5.99	6.95	4.64
Velocity (mm/μs)	6.32	4.13	4.13	4.20	3.63	6.57
Acoustic curvature factor (b)	0.24	0.73	0.49	0.19	-0.12	-0.20
Acoustic curvature (1-2b)	0.53	-0.45	0.03	0.62	1.23	1.39
AO figure of merit (M2) (E15s3/kg)	44.60	24.75	24.75	34.50	36.10	6.95
Attenuation (dB/μs/GHz^2)	3.00	1.50	1.50	6.00	5.45	1.00
Optical wavelength (nm)	820.00	820.00	820.00	820.00	820	820
INPUT VALUES						
Center frequency (MHz)	165.00	165.00	165.00	165.00	165.00	165.00
Bandwidth (MHz)	110.00	110.00	110.00	110.00	110.00	110.00
Time aperture (μs)	1.00	1.00	1.00	1.00	1.00	1.00
CALCULATED VALUES						
Acoustic wavelength at F0 (μm)	38.30	25.03	25.03	25.45	22.00	39.82
Transducer length (μm)	15989.84	6828.26	6828.26	4821.58	3802.47	11485.12
Transducer height (μm)	357.51	215.68	51.84	257.46	313.41	603.02
Bragg angle (external) (mrad)	10.70	16.38	16.38	16.11	18.64	10.30
Bragg angle (internal) (mrad)	3.23	4.95	4.95	7.13	7.81	4.68
Acousto-optic efficiency (%/mW)	1.46	0.57	2.37	0.47	0.32	0.10
Attenuation loss	0.98	1.00	1.00	0.98	0.98	1.00
Tranducer insertion loss	0.50	0.50	0.50	0.50	0.50	0.50
Total diffraction eficiency (%/mW)	0.71	0.29	1.19	0.23	0.16	0.05
Diffraction efficiency at 100 mW (%)	55.94	25.99	78.70	21.50	14.98	4.76
Diffraction efficiency at 1W (%)	20.49	98.55	9.24	99.79	90.47	41.09

Table III is arranged in 3 parts. The top part gives the material parameters of the acousto-optic mode under consideration. Of particular interest here is the acoustic curvature $C = 1 - 2b$. The acoustic curvature measures the acoustic anisotropy of the material and hence is a measure of the diffraction spreading of the acoustic waves from the transducer. It is an important

70

parameter when a multichannel device design is under consideration because it governs the degree to which two channels can be closely spaced without deleterious crosstalk over the time-aperture of the cell. C = 1 indicates the material is isotropic. When C is 0 the material is said to be self-collimating and very little diffraction spreading occurs. The shear mode in GaP with optical illumination along the [111] direction has this property. The analysis shows that TeO_2 mode is the most efficient and, if our objective was to develop a single channel device, it would be the mode of choice. The third GaP mode in the table, the self-collimating mode, delivers an order of magnitude lower efficiency. Nevertheless this lower performance may be mitigated by its diffraction spreading performance. Continuing the investigation of designs for multichannel Bragg cells, we compared the crosstalk performance of 6 different 107 MHz bandwidth, 1 μs time-aperture acousto-optic Bragg cell designs. We investigated designs using three different acoustic modes in Gallium Phosphide (GaP), as well as modes in Tellurium Dioxide (TeO_2), Lead Molybdate ($PbMoO_4$), and Lithium Niobate ($LiNbO_3$). The results of this calculation are shown in Fig 7. We first normalized the transducer height of each of the Bragg cell designs to the acoustic wavelength and then calculated the acoustic diffraction profile a distance in wavelengths equal to 1 μs time-aperture from the transducer. The GaP self collimating mode, with a normalized height of 2 wavelengths, shows the narrowest acoustic beam, as expected. The -30 dB point in the profile occurs at a distance of about 50 wavelengths from the center of the transducer. The other GaP modes show -30 dB intensities at slightly larger distances away. The other 3 modes have -30 dB intensities some 125 wavelengths away. The normal GaP shear mode does not perform significantly worse than the self collimating shear mode yet it has a factor of 10 improvement in diffraction efficiency over the self-collimating mode. From this analysis we find that the GaP normal shear mode is the optimum approach for this application. A single channel device of this type is commercially available from Brimrose Corporation (model GPD-25-10) [11]. It has an efficiency of 50% with an active aperture is 0.75 × 5 mm.
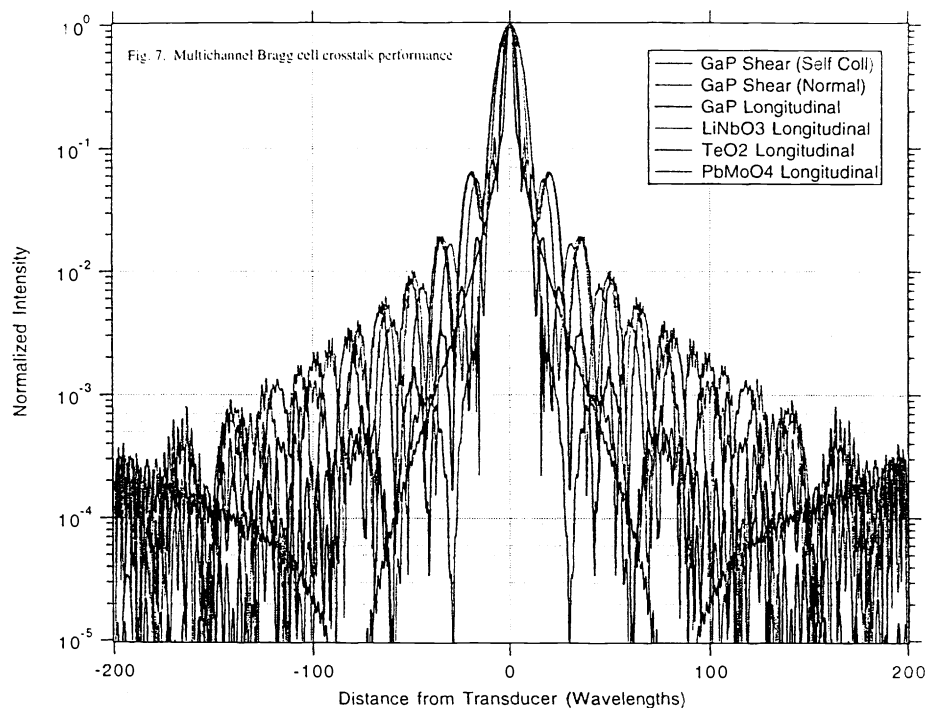

Figure 7: Multichannel Bragg cell crosstalk performance.

3.3 Lenses

In this section each of the lens elements in Fig. 2 are specified in terms of focal length. Referring to the side view of the processor, Fig. 3, the cylindrical lens C1y compresses the collimated laser beam in the transducer dimension of AOD1 so that the beam is efficiently diffracted by AOD1's acoustic beam. We assume that AOD1 has an aperture of 0.076 mm × 5 mm, as discussed above. To obtain good acousto-optic coupling efficiency, the height of the beam at AOD1 should be approximately 80% of the transducer height - thus a beam diameter of approximately 0.06 mm (ω_0) is needed. Assuming we have a 5 mm diameter (W) collimated 690 nm wavelength laser beam, a simple spherical lens would require a focal length of:

71

$$F_{Cly} = \frac{W \cdot \omega_o}{1.27 \cdot \lambda} = 342 \text{mm} \qquad (15)$$

The working distance of this lens can be reduced using a cylindrical telephoto lens assembly. A factor of 4 reduction in working distance is easily achievable and thus a working distance of about 85 mm is required. Lens S1 compresses both the diffracted and undiffracted beams exiting AOD1 in the horizontal (top view) dimension and collimates the beam in the vertical (side view) dimension so that the two beams pass through Bragg cells AOD3 and AOD4, respectively. These cells, as discussed above, have apertures of 0.75 × 5 mm. Because the transducer dimension is large (0.75 mm) it is convenient to use an anamorphic prism pair here to reduce the beam width from 5 mm to 0.6 mm in the horizontal dimension. Prism pairs of this type are commercially available, from, for example, Melles Griot, with lengths of about 33 mm [12]. In the orthogonal dimension we require a cylindrical lens with the same focal length as C1y (which has a working distance of 85 mm). Lens S2 must recollimate the beam in the horizontal dimension (top view) and focus it in the vertical dimension (side view) to pass through AOD2. Since AOD2 has the same aperture as AOD1, we will use the same arrangement here as for S1, an anamorphic prism pair and cylindrical lens. Lens C2y, in combination with S2, images the 5 mm length cells AOD3 and AOD4 onto the CCD array. The length of the CCD array in this dimension is (see discussion in the next section) 24 pixels × 30 μm = 0.72 mm. Thus we need to demagnify AOD3 and AOD4 by a factor of about 7 and so the focal length of C2y must be $1/7 \times F_{C1y} = 49$ mm. Lenses C2x and C1x are arranged to image the 5 mm length AOD2 onto the orthogonal dimension of the CCD array. The length of the CCD array in this dimension is (see discussion in the next section) 200 pixels × 18 μm = 3.6 mm. Thus we need to demagnify AOD2 by a factor of about 1.4 and so the ratio of the focal lengths of C2x to C1x must be 1.4. For convenience we make the focal length of C1x 25 mm and the focal length of C2x 35 mm. The CCD will be located just behind C2x. The total optical path length of the processor, as summarized in Fig. 8, is about 430 mm.
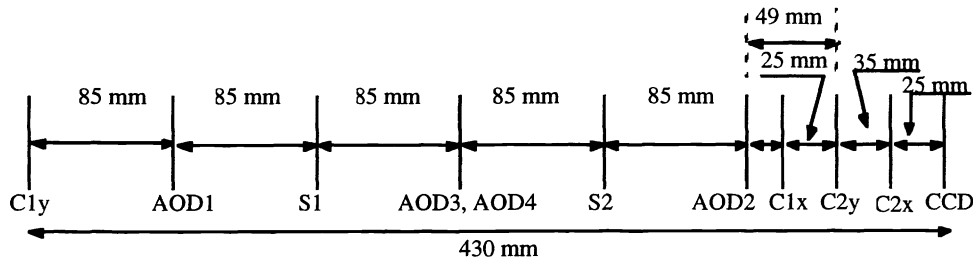

Figure 8: Optimized ISAR optical processor optical path length design.

3.4 Photodetector Array

The ISAR image is formed directly on the CCD photodetector array. Nominally we would require 1 photodetector element in each dimension of the array for each range and Doppler bin. However, as shown in Eq. (8), the light intensity on the array is on a spatial carrier. In order to recover the image, then, we must sample the spatial carrier with at least 2 pixels per bin. Since 100 range × 24 Doppler bins are needed, we require a CCD with a minimum dimension of 200 × 48 elements. High performance CCD arrays are commercially available from a number of sources with pixel dimensions well in excess of this requirement. An example is the Loral Fairchild CCD 222, a 488 × 380 high dynamic range array with low light level performance and video data rates up to 20 Megapixels/sec [13]. The pixel dimensions of this array are 12 μm horizontal by 18 μm vertical on 30 μm horizontal centers and 18 μm vertical centers.

3.5 Light Source

We require a light source that is small and low power consuming and that provides sufficient light intensity to utilize the full dynamic range of the CCD detector. In the following light budget calculation we determine the minimum required light source power. The CCD 222 has a well capacity of approximately 500,000 electrons (limited by the blooming in the read-out registers). The quantum efficiency at 690 nm is 35%. The total number of photons/pixel required to fill a well is therefore 500,000 electrons/0.35 = 1,428,571 photons/pixel. Each pixel is illuminated for a time equal to the compressed pulse length (2 ns) × the total number of pulses during the 0.5 s integration period (5 kHz PRF × 0.5 s = 2,500 pulses) = 5 μs. For a 200 × 48 element array, with an integration time of 5 μs, we require, at the CCD array, an optical power of 1,428,571 photons/pixel × 9,600 pixels/5 μs = 2.75 × 10^{15} photons/sec. The optical power required at the CCD array to saturate all pixels is therefore 2.75 × 10^{15} hc/l = 0.8 mW at a wavelength of 690 nm. Since the optical beam passes through 4 Bragg cells, each with efficiency of about 10%, we assume an intensity loss factor of 0.01. We thus require (assuming no other losses) a source with 80 mW of optical power. Allowing some optical loses, a source with 100 mW of power is

72

adequate for this processor. A number of commercial vendors supply high performance laser diodes with output at 690 nm with optical powers exceeding 100 mW.

3.6 Electronic Subsystem

The AO ISAR processor requires a set of control electronics similar to that of any standard AO processor. That is, a laser diode controller is needed which maintains the laser diode at constant output power and temperature (to prevent mode hoping). Each Bragg cell requires a driver with an adjustable carrier offset frequency. The CCD requires standard integration and read-out control electronics. Of particular interest, however, is the electronic circuitry to extract the ISAR image.

The ISAR image is corrupted by bias terms and is itself on a spatial carrier. A quadrature detection circuit, as shown in Fig. 9, can be used to extract the image. The image I read out serially from the CCD is split into two channels. In the top channel the signal is multiplied by the cosine of the spatial frequency while in the bottom channel it is multiplied by the sine of the spatial frequency. If we filter this signal with a low pass filter the result is a signal independent DC term and the term of interest. The signal independent bias term can be measured a priori and then subtracted from the image term electronically.
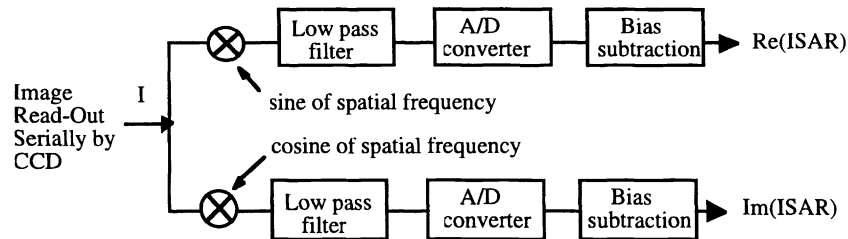

Figure 9: Quadrature Detection Circuit.

4. PROOF OF CONCEPT EXPERIMENTS

Using available components, the ISAR AO processor was breadboarded on an optical bench (without air floatation) in the Photonic Information Processing Systems (PIPS) Laboratory at CREOL - University of Central Florida. All of the Bragg cells or AODs were Intraaction Corp. flint glass devices with a 70 MHz center frequency, 40 MHz bandwidth, 3.9 mm/μsec acoustic velocity, and 10 μsec time-aperture. Based on the laser module compactness and weight, light level stability, and ease in availability, the PIPS Lab's high power 532 nm, 100 mW output power diode-pumped CW Nd:YAG laser was used. The light was spatially filtered using a 25 μm pin-hole, 10× microscope assembly. The filtered laser light is designed to be collimated by a 15 cm focal length (FL) spherical lens S, forming a 22 mm diameter collimated optical beam. The collimated beam was focused into AOD1 using a 30 cm FL cylindrical lens C1y. Spherical lenses S1 and S2 with 50 cm focal lengths formed the required 1 : 1 imaging system between the AOD1 and AOD2 planes. The large 50 cm FL of S1 was used to ensure that the diffracted (+1 order) and undiffracted (DC) beams from AOD1 have adequate spatial separation in the front focal plane of lens S1, such that the undiffracted beam is positioned within the acoustic column of AOD4, and the diffracted beam is positioned in AOD3. The large separation between the DC and +1 order beams from AOD1 is required as the PIPS Lab. flint glass AODs have large (4 mm) acoustic beam height dimensions (or cell thickness), preventing AOD4 and AOD3 to be positioned very close (e.g., 0.2 mm) apart. The DC light beams from AOD4 and AOD3 were blocked by the metallic casing of AOD2, which acts as a DC block. The undiffracted light beam from AOD2 was blocked in the front Fourier plane of cylindrical lens C1x with FL=20 cm. The cylindrical lens C2y of FL=30 cm and the sphere S2 of FL=50 cm form an imaging system along the y-direction with a magnification My=30/50=0.6. Here, the AOD4/AOD3 plane is imaged along the y-direction on to the processor output plane where a 2-D Sony CCD was positioned. This Black and White Sony CCD is a Model XC-77 device with 384 horizontal pixels with a 23 micron pixel separation, and 491 interlaced pixels with a 13.4 micron separation in the vertical direction. The 10 cm FL cylinder C2x and the cylinder C1x form an imaging system along the x-direction with a magnification Mx=10/20=0.5. Here, AOD2 plane was imaged along the x-direction on-to the processor output plane. All the signals driving the AODs were mutually phase coherent as all signal generators that were used in the experiment were externally locked to a stable 10 MHz reference oscillator. The RF equipment used included a Tektronix Model 11801B Oscilloscope, two Wavetek Model 5135A Signal Synthesizers, 1 HP Model 83752A Sweep Synthesizer, and a Tektronix Model 2710 RF spectrum analyzer.

Because all temporal information input via the 4 Bragg cells in the ISAR AO processor are converted to spatial frequency information at the output CCD plane, the processor can be fully characterized in terms of signal processing capability (e.g.,

73

system bandwidths and processing resolution) by simply observing the output spatial frequency information. Hence, first we feed single tone signals to the 4 Bragg cells. By using different frequency tones that are mutually phase coherent, we can generates any desired fringe pattern at the CCD. For instance, by controlling the frequency difference between the AOD1 and AOD4 x-direction cells, we generate a spatial carrier in the x-direction. Fig. 10 shows these results both in image form and as a video line trace. Note the excellent fringe visibility or modulation depth (Fig. 11) shows the zero light level of the video line for comparison), considering that this proof-of-concept AO processor design is physically very large and built on a table with no air isolation or other precautions. Fig. 12 similarly shows a typical spatial carrier in the y-direction. This is generated by controlling the frequency difference between the AOD2 and AOD3 y-direction cells. Again note the excellent fringe visibility. Note that it is also possible to simultaneous generate spatial carriers in both the x and y-direction. This is done by introducing a desired frequency difference between the AOD2 and AOD3 y-direction cells, and a desired frequency difference between the AOD1 and AOD4 x-direction cells. If these frequency differences are equal (as in Fig. 13), a + 45 degree fringe pattern can also be introduced by our processor. Recall from our processor theory that to observe a stationary fringe pattern on the CCD, we must make sure that the net Doppler shifts of the diffracted beams add to be zero on interferometric detection via the time integrating CCD. Next, we examine what is the maximum spatial frequency our AO processor can generate along the x and y processing directions of the CCD. Again, this is done by introducing a frequency difference between the AOD2 and AOD3 y-direction cells, and then between the AOD1 and AOD4 x-direction cells. Fig. 14 shows a typical fast carrier observed in the x-direction for a 60 MHz frequency difference. Similarly, Fig. 15 shows a typical fast carrier observed in the y-direction for a 40 MHz frequency difference. Based on $2\times$ Nyquist sampling, this means that we can process 30 MHz bandwidth spread signals along the processor output plane x-direction, while we can process 20 MHz bandwidth spread signals along the processor output plane y-direction. These results are impressive considering that the Bragg cells are designed by the manufacturer to operate from 50-90 MHz (3-dB bandwidth) and a 70 MHz center frequency. Hence, large fractional bandwidths (e.g., > 50 %) are possible with our processor design.
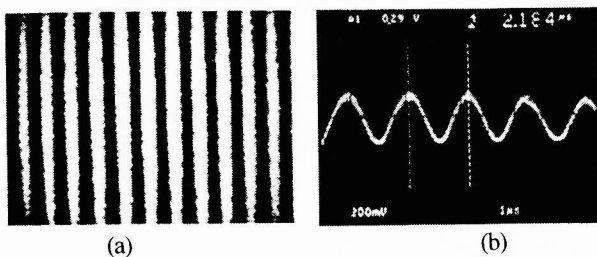

(a) (b)

Figure 10: Spatial carrier in x direction: a) image and b) video trace showing a 2.75 cycles/mm carrier.
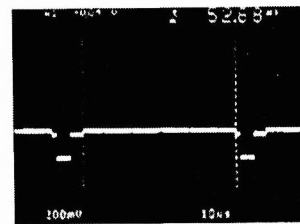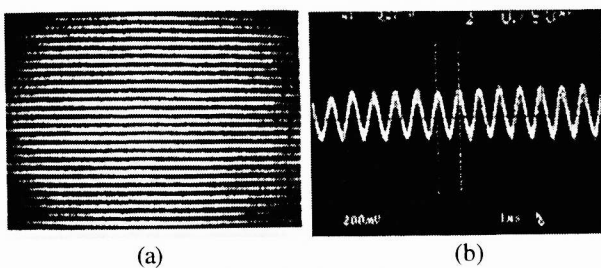

Figure 11: Video line with zero light level

(a) (b)

Figure 12: Spatial carrier in y direction: a) image and b) video trace showing a 7.5 cycles/mm carrier.
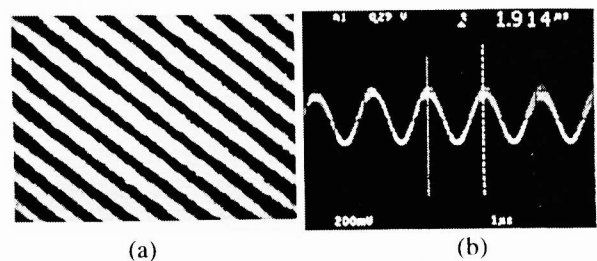

(a) (b)

Figure 13: Spatial carrier in x and y (45°) direction: a) image and b) video trace showing a 3.16 cycles/mm carrier in x and y.

Furthermore, by looking at the maximum spatial frequencies along the x and y directions of the CCD, we can estimate the processed signal resolution bins. For example, for a 2-D range (in x) and Doppler (in y) CCD output plane format, the one spatial cycle in the x-direction gives one range resolution bin while one spatial cycle in the y-direction gives one Doppler resolution bin. In our laboratory system, we experimentally estimate this one full fringe cycle (at the max. spatial frequency) to be approximately 5 CCD pixels in the x-direction and 6 CCD pixels in the y-direction (see video line trace photos where 1 video line (about 8.8 mm) is 52.84 microseconds. Hence, by measuring the spatial cycle temporal period, we can estimate the physical size of the spatial fringe cycle at the CCD plane.

One way to test our AO processor is via implementing autocorrelations of various test signals. First, we implement an autocorrelation in the x-direction, then an autocorrelation in the y-direction. We use AM signals. These preliminary experimental results shown in Figures 16-17 indeed show the large processing power of our AO system.
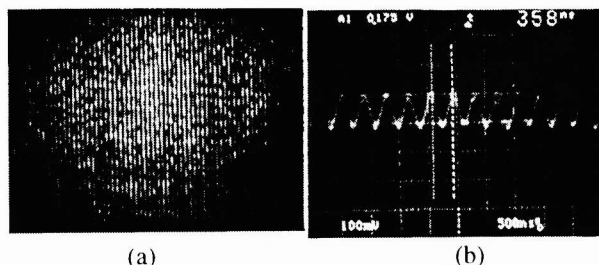

(a)   (b)

Figure 14: Fast carrier in x direction (60 MHz difference): a) image and b) video trace showing a 16.8 cycles/mm maximum carrier.
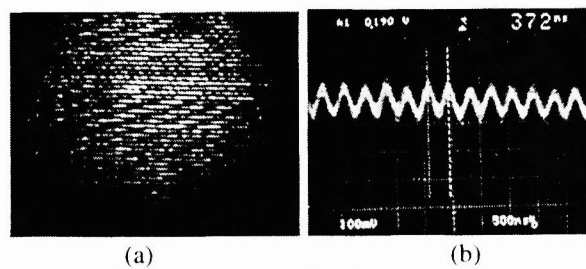

(a)   (b)

Figure 15: Fast carrier in y direction (40 MHz difference): a) image and b) video trace showing a 16.2 cycles/mm maximum carrier.
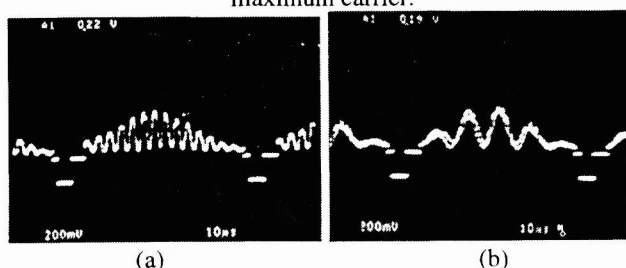

(a)   (b)

Figure 16: Autocorrelation of an AM signal in x direction (90 MHz carrier): a) 3 MHz modulation frequency and b) 1 MHz modulation frequency. Output not on a spatial carrier.
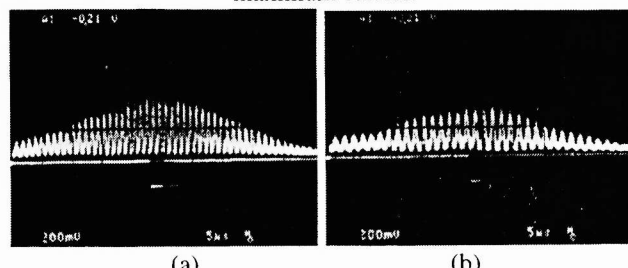

(a)   (b)

Figure 17: Autocorrelation of an AM signal in y direction (90 MHz carrier): a) 7 MHz modulation frequency and b) 5 MHz modulation frequency. Output not on a spatial carrier.

The important results from these proof of concept experiments are: (a) A moderate power (e.g., 100 mW) laser is sufficient for processor operation, even though 4 Bragg cell diffractions are used. (b) The processor shows excellent phase stability, even though the lab. system design is large and bulky and no air isolation is used. (c) The processor offers excellent > 50% fractional bandwidths for radar signal processing. (d) The processor offers excellent fringe modulation depths for carrier based output demodulation.

5. CONCLUSION

The research effort described in this paper has resulted in an innovative acousto-optic signal processing architecture for ISAR ship image formation that is ideally suited to airborne applications where size, weight, and power are important performance parameters. We developed the specifications for the ISAR image formation processor for ship imaging based upon the Texas Instruments AN/APS-137(H) Airborne Radar. The baseline processor is designed for high resolution imaging - slant range resolution of 0.3 m and cross range resolution of 1.2 m over a 30 m × 30 m window. We developed the specifications for the optoelectronic components for the processor, including light source, lenses, photodetector array, and Bragg cells including a mutichannel Bragg cell to improve processor bandwidth and reduce its size. We showed that all of these components are commercially available. We breadboarded a narrow bandwidth version of the processor and demonstrated its main operating features. We showed that the processor does indeed have simultaneous spatial carrier generation capability that is controllable with high phase stability and excellent fringe visibility.

6. ACKNOWLEDGEMENT

7. REFERENCES

1. N. A. Riza, "Multi-function acousto-optic signal processor," in *Advances in Optical Information Processing VIII*, D. R. Pape, Ed., Proc. SPIE, Vol. 3388, April 1998.
2. N. A. Riza, "High speed two dimensional phased array antenna scanning using acousto-optics," in *Opto-Electronic Signal Processing for Phased Array Antennas III* , Proc. SPIE, Vol. 1703, pp. 460-468, 1992.
3. N. A. Riza, "Acousto-optic architecture for two dimensional beam scanning in phased array antennas," *Applied Optics* , Vol. 31, No. 17, pp.3278- 3284, June 10, 1992.
4. N. A. Riza, "Experimental demonstration of an acoustooptic system for two dimensional phased array antenna scanning," *Applied Optics* , Vol. 32, No. 11, pp. 1936-1942, April 10, 1993.
5. Ausherman, et. al, "Developments in Radar Imaging," *IEEE Trans. on Aerospace and Electron. Sys.*, Vol. AES-20, No. 4, pp. 363- 400, 1984.
6. V. C. Chen, "Radar ambiguity function, time-varying matched filter, and optimum wavelet correlator," *Optical Engineering*, Vol. 33, No. 7, pp. 2212-2217, July 1994.
7. Donald R. Wehner, *High Resolution Radar*, Chapter 7, Artech House, Norwood, MA, 1987.
8. H. Szu, Y. Sheng, J. Chen, "Wavelet transform as a bank of matched filters," *Applied Optics*, 31, 3267-3277 (1992).
9. Jane's Radar and Electronic Warfare Systems, 1995 - 1996, ed. Bernard Blake, Jane's Information Group Inc, Alexandria, VA 1995.
10. D. Curtis Schleher, *MTI and Pulsed Doppler Radar*, Chapter 8, Artech House, Norwood, MA, 1991.
11. Brimrose Acousto-Optics Products catalog, Brimrose Corporation, Baltimore, MD, January, 1992.
12. Melles Griot catalog, Melles Griot Inc., Irvine, CA, 1995.
13. Loral Fairchild CCD Databook, Loral Fairchild Imaging Sensors, Milipitas, CA, 1994.